Applied Catalysis B: Environmental 181 (2016) 236–248

Contents lists available at ScienceDirect

Applied Catalysis B: Environmental

journal homepage: www.elsevier.com/locate/apcatb

Pd–Co based spinel oxides derived from pd nanoparticles immobilized on layered double hydroxides for toluene combustion

Shen Zhao, Kezhi Li, Su Jiang, Junhua Li*

State Key Joint Laboratory of Environment Simulation and Pollution Control, School of Environment, Tsinghua University, Beijing 100084, China

ARTICLE INFO

Article history:
Received 7 June 2015
Received in revised form 31 July 2015
Accepted 4 August 2015
Available online 6 August 2015

Keywords:
Spinel oxides
Layered double hydroxides
Toluene combustion

ABSTRACT

Noble metal nanoparticles (noble metal NPs, noble metal = Ag, Pt and Pd) have been successfully immobilized on CoAl-layered double hydroxide (CoAl-LDHs) layers using a simple and facile self-redox process to afford noble metal NPs immobilized on CoAl-LDHs (N–CoAl-LDHs, N = Ag, Pt and Pd). In addition, the CoAl-LDHs and N-CoAl-LDHs were calcined in air at 600 °C to afford the CoAlO and N-CoAlO catalysts for toluene combustion. The catalytic and characterization results indicated that the Pd–CoAlO catalyst exhibited the highest catalytic activity because it possessed the highest low-temperature reducibility and the most abundant surface Co^{3+} and surface adsorbed oxygen species. In addition, the noble metal NP sizes of the N–CoAlO catalysts affected the catalytic activity for toluene combustion, and the existence of catalytically active PdO contributes to the excellent catalytic activity of the Pd–CoAlO catalyst for toluene combustion. The comparison experiments reveal that the PdO phase and CoAlO support play significant role in the toluene combustion and they participate cooperatively in the reaction process. In addition, the *in situ* DRIFTS results indicated that the benzoate species are the main intermediate species in toluene combustion, which should be further oxidized by O_2 to the final products (*i.e.*, CO_2 and H_2O).

1. Introduction

Volatile organic compounds (VOCs) produced by industrial manufacturing are a significant class of air pollutants. Many environmental problems, such as offensive odors, toxic emissions, ozone formation and petrochemical smog, are related to the emission of VOCs. In the last few decades, many technologies for VOC abatement have been developed including thermal oxidation, catalytic oxidation and adsorption [1]. Among these techniques, catalytic oxidation is regarded as an effective method for VOC abatement because (1) it has a higher destructive efficiency than adsorption, (2) it has a lower operating temperature and less harmful reaction by-products than thermal oxidation, and (3) it does not require additional fuel, reducing energy consumption and avoiding the formation of thermal NO_x [2]. The key issue in catalytic oxidation technology is the availability of a highly active catalyst. Although various transition metal oxides and mixed metal oxides exhibit good catalytic performance for VOC combustion [3], supported noble metals are the most desirable catalysts due to their excellent low temperature activity [4].

Supported Pd catalysts exhibit excellent low temperature activity for VOC combustion [4b,4c,4f,5]. The two key factors that affect the catalytic activity of supported Pd catalysts are as follows: (1) the Pd oxidation state because PdO is more active than metallic Pd for VOC combustion [5a,5b] and (2) the textural properties of the support, which influence the dispersion of the Pd active species [5c,5d]. Although supported Pd catalysts have been widely used in VOC combustion, the two serious problems that restrict their further application are as follows: (1) traditional preparation methods involve tedious procedures and require reducing agents and (2) highly homogeneous and thermally stable dispersions of Pd nanoparticles (Pd NPs) are difficult to achieve on supports using traditional preparation methods. To solve these challenges, a support with evenly distributed reductive sites that can *in situ* reduce Pd^{2+} and disperse Pd NPs is needed. Layered double hydroxides (LDHs) have the potential to be an ideal support for Pd NPs.

Layered double hydroxides (LDHs) or hydrotalcite-like compounds are a large family of two-dimensional (2D) anionic clay materials that are represented by the general formula $[M_{1-x}^{2+}M_x^{3+}(OH)_2]^{x+}[A_{x/n}]^{n-}\cdot mH_2O$, where M^{2+} and M^{3+} are di- and trivalent metal cations, respectively, A^{n-} is a counteranion, and

* Corresponding author. Fax: +86 10 62771093.
E-mail address: lijunhua@tsinghua.edu.cn (J. Li).

http://dx.doi.org/10.1016/j.apcatb.2015.08.001
0926-3373/

$x = 0.17–0.33$ defined by $M^{3+}/(M^{2+} + M^{3+})$ ratio [6]. Cobalt-based LDHs are ideal supports due to homogeneously distributed reductive Co^{2+}. A highly homogeneous and thermally stable dispersion of Pd NPs on cobalt-based LDHs can be achieved *via* an *in situ* redox reaction between the reductive cobalt-based LDH supports and the oxidative Pd^{2+} precursors [7]. Therefore, the resulting Pd NPs immobilized on cobalt-based LDHs can be used as ideal catalyst precursors for VOC combustion due to the highly homogeneous and thermally stable dispersion of Pd NPs on the LDH supports. The transformation of the LDH precursors into spinel oxides is topotactic due to the ordering and uniform distribution of metal cations in the layers. The obtained spinel oxides have two advantages over those produced using traditional methods: (1) the specific surface areas are typically large and (2) highly homogeneous and thermally stable dispersion of metal ion components can be achieved. In addition, the structures and properties of the obtained spinel oxides can be tuned by changing the composition of the LDH precursors [8]. Therefore, the cobalt-based LDHs are ideal supports for Pd NPs, and the resulting Pd NPs immobilized on cobalt-based LDHs can be further transformed to Pd–Co based spinel oxide catalysts for VOC combustion.

Based on this strategy, we have successfully immobilized a series of noble metal nanoparticles (*i.e.*, Ag, Pt and Pd NPs) on $Co_{0.66}Al_{0.34}(OH)_2(CO_3)_{0.17}{\cdot}0.71H_2O$ (CoAl-LDHs) layers through a simple and facile *in situ* redox process [7]. In addition, the CoAl-LDHs and noble metal NPs immobilized on CoAl-LDHs (N–CoAl-LDHs, N = Ag, Pt and Pd) were calcined in air at 600 °C to afford the corresponding CoAlO, Ag–CoAlO, Pt–CoAlO and Pd–CoAlO catalysts for toluene combustion. The catalytic and characterization results indicated that the Pd–CoAlO catalyst exhibited the highest catalytic activity because it possessed the highest low temperature reducibility as well as the most abundant surface Co^{3+} and surface adsorption oxygen species. The comparison experiments reveal that the PdO phase and CoAlO support play significant role in the toluene combustion and they participate cooperatively in the reaction process. In addition, the noble metal NP sizes of N–CoAlO affected the catalytic activity of toluene combustion, and the existence of catalytically active PdO contributes to the excellent catalytic activity of the Pd–CoAlO catalyst for toluene combustion. In addition, the *in situ* DRIFTS results indicated that the benzoate species are the main intermediate species in toluene combustion, which should be further oxidized by O_2 to the final products (*i.e.*, CO_2 and H_2O).

2. Experimental

2.1. Chemical materials

Cobalt nitrate hexahydrate ($Co(NO_3)_2{\cdot}6H_2O$), aluminum nitrate nonahydrate ($Al(NO_3)_3{\cdot}9H_2O$), urea, silver nitrate ($AgNO_3$), sodium hexachloroplatinate hexahydrate ($Na_2PtCl_4{\cdot}6H_2O$), sodium tetrachloropalladate (Na_2PdCl_4), cobalt oxide (Co_3O_4) and aluminum oxide (Al_2O_3) were purchased from Sigma-Aldrich and used without further purification.

2.2. Measurements

The powder X-ray diffraction (XRD) patterns were measured on an X-ray diffractometer (Rigaku, D/max-2200, Japan) equipped with a Cu Kα radiation source (λ = 0.15405 nm, 40 kV and 200 mA). The scanning range was 3–70° at a step of 10° min^{-1} with a step size of 0.02°. The Raman spectra were measured on a Microscopic Confocal Raman Spectrometer (Renishaw, RM2000) under ambient conditions using a laser with a wavelength of 532 nm. The spectra were recorded at a resolution of 1 cm^{-1} using a scan number of 20 from 40 to 1300 cm^{-1}. Transmission electron microscopy (TEM) images were recorded on a JEM-2011 instrument at a voltage of 200 kV. The samples were prepared by ultrasonic dispersion in ethanol and dispersed for several minutes, and the transparent suspended droplets were placed on a copper grid using a capillary. Thermogravimetric analysis (TGA) was performed on a TGA/DSC 1 STARe from Mettler Toledo in flowing air from 50 °C to 800 °C with a heating rate of 10 °C/min. Inductively coupled plasma-atomic emission spectroscopy (ICP) analysis was performed using a Thermo IRIS spectrometer. The N_2 adsorption-desorption experiments were performed on a Quantachrome Autosorb-1 instrument at liquid N_2 temperature (−196 °C). The samples were outgassed at 300 °C for 4 h prior to N_2 adsorption. The temperature-programmed reduction of hydrogen (H_2-TPR) was carried out on a chemisorption analyzer (Micromeritics, ChemiSorb 2720 TPx). The samples were pretreated at 300 °C for 1 h prior to each experiment. Then, the samples were cooled to 50 °C in a flow of N_2. The reduction of the samples was initiated from 50 to 1000 °C with a mixture of 10% H_2/Ar (50 ml/min) at a rate of 10 °C/min. The consumption of H_2 was continuously monitored using a thermal conductivity detector (TCD). The H_2 consumption of the reduction band was calibrated by a standard CuO (99.998%) powder. The CO–TPD was also tested on the above instrument. Portions (0.05 g) of samples were treated at room temperature with 50 ml/min of 5% CO/N_2 for 1 h. The temperature was programmed to increase to 450 °C at a rate of 10 °C/min after the samples adsorbed enough CO. X-ray photoelectron spectroscopy (XPS) analysis was performed on a PHI-5300/ESCA electron spectrometer from VG Scientific using 300 W Mg Ka radiation. The base pressure was approximately 3×10^{-9} mbar. The binding energies of all of the elements were referenced to the C 1s line at 284.8 eV from carbon impurities. The data were processed using the XPS-PEAK software. The *in situ* DRIFTS experiments were recorded with a Nicolet Nexus spectrometer equipped with a liquid nitrogen-cooled MCT detector. A Praying Mantis™ High Temperature Reaction Chamber from Harrick Scientific Products Inc. was used as an environmental chamber, and a dome with two KBr windows and one glass observation window were used in the chamber. The samples were placed onto a sample cell in an atmospherically controllable chamber for DRIFTS spectroscopic analysis. Circulating water kept the outside of the chamber cool when operating at high temperatures. Prior to each experiment, the catalyst was heated at 300 °C in a flow of N_2 (100 ml/min) for 60 min. The FT-IR spectra were recorded by accumulating 100 scans at a resolution of 4 cm^{-1}.

2.3. Preparation of CoAl-LDHs [9]

A 200-ml mixture consisting of $Co(NO_3)_2{\cdot}6H_2O$ (5.82 g, 0.02 mol), $Al(NO_3)_3{\cdot}9H_2O$ (3.75 g, 0.01 mol), and urea (6.00 g, 0.10 mol) was prepared, and after filtration, the solution was placed in autoclave bombs. The autoclave bombs were heated at 110 °C for 24 h. The products were filtered, washed with ethanol and water, and dried in air. Based on the TGA and ICP analyses, the formula of CoAl-LDHs was determined to be $Co_{0.66}Al_{0.34}(OH)_2(CO_3)_{0.17}{\cdot}0.71H_2O$.

2.4. Preparation of Ag-CoAl-LDHs [10]

CoAl-LDHs (1.00 g, 9.52 mmol) were dispersed in 100 ml of a 0.05 M $AgNO_3$ aqueous solution. Then, the resulting suspension was heated at 100 °C for 3 h. The products were filtered, washed with ethanol and water, and dried in air. Based on the TGA and ICP analyses, the formula of Ag–CoAl-LDHs was determined to be $Ag_{0.096}Co_{0.66}Al_{0.34}(OH)_2(CO_3)_{0.17}{\cdot}0.72H_2O$ (8.96 wt.% Ag).

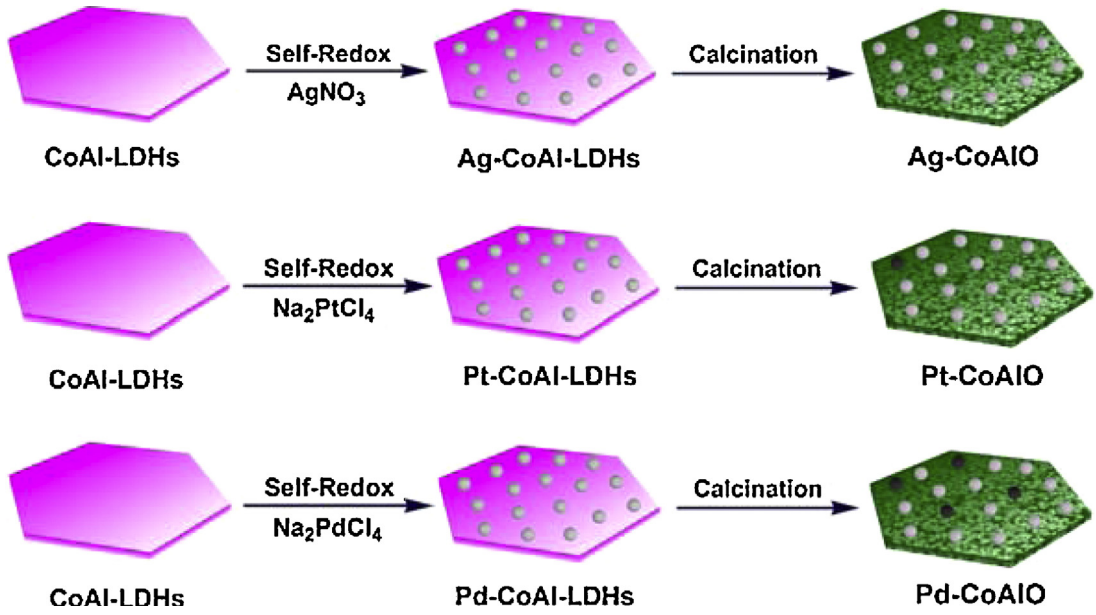

Scheme 1. Preparation process for N–CoAl-LDHs and N–CoAlO.

2.5. Preparation of Pt/Pd–CoAl-LDHs [7]

CoAl-LDHs (0.20 g, 1.91 mmol) were dispersed in 200 ml of water. Then, 1.40 ml of a 5.64×10^{-2} M Na_2PtCl_4 or Na_2PdCl_4 aqueous solution was added to this CoAl-LDH suspension under vigorous stirring. After 12 h of stirring at 25 °C, the products were filtered, washed with ethanol and water, and dried in air. Based on the TGA and ICP analyses, the formulas of Pt–CoAl-LDHs and Pd–CoAl-LDHs were determined to be $Pt_{0.018}Co_{0.66}Al_{0.34}(OH)_2(CO_3)_{0.17}{\cdot}0.38H_2O$ (3.42 wt.% Pt) and $Pd_{0.034}Co_{0.66}Al_{0.34}(OH)_2(CO_3)_{0.17}{\cdot}0.68H_2O$ (3.35 wt.% Pd), respectively.

2.6. Preparation of CoAlO and N-CoAlO (N = Ag, Pt and Pd)

The CoAlO and N–CoAlO catalysts were obtained by calcining the CoAl-LDH and N–CoAl-LDH precursors in air at 600 °C for 4 h.

2.7. Catalytic evaluation

The evaluation of the catalytic activity was conducted in a fixed-bed quartz tubular microreactor (Φ = 10.0 mm) with 0.10 g of catalyst (40–60 mesh). Toluene gas was generated and injected using a N_2 bubbler in a low temperature thermostatic bath at 0 °C, which passed through a container filled with toluene. The volumetric composition of the reactant mixture was 2000 ppm toluene + 20% O_2 + balance N_2, and the total flow was 100 ml/min, which affords a gas hourly space velocity (GHSV) of 60,000 ml/(g h). The range of test temperatures was 180 to 330 °C. The concentrations of the reactants and products were monitored on line by a gas chromatograph (Agilent 7890A) equipped with FID and TCD detectors using the Porapack-Q and HP-INNOWAX columns, respectively. No carbon products other than CO_2 were detected. The toluene conversion ($X_{toluene}$), turnover frequency per surface Co^{3+} (TOF_{Co}) and noble metals (TOF_N, N = Ag, Pt and Pd) were calculated according to the following equations [4d]:

$$X_{toluene} = \frac{(c_{in} - c_{out})}{c_{in}} \times 100\% \quad (1)$$

$$TOF_{Co} = \frac{C_{toluene} X_{toluene} V_{gas}}{n(Co^{3+})} [s^{-1}] \quad (2)$$

$$TOF_N = \frac{C_{toluene} X_{toluene} V_{gas} M_N}{m_{Cat} w_N D_N} [s^{-1}] \quad (3)$$

where c_{in} and c_{out} are the toluene concentration corresponding to the inlet and outlet, respectively, V_{gas} is the total molar flow rate, $C_{toluene}$ is the concentration of toluene in the gas mixture, $n(Co^{3+})$ is the number of moles of Co^{3+} per gram of the CoAlO and N-CoAlO catalysts calculated by H_2-TPR, M_N, the atomic weight of noble metals (*i.e.*, Ag, Pt and Pd); m_{cat} is the mass of catalyst in the reactor bed; w_N, the mass fraction of noble metals tested by ICP (Table S5); D_N, the dispersion of noble metals estimated by CO chemical adsorption (Table S5).

3. Results and discussion

3.1. Preparation and characterization of N–CoAl-LDH precursors

N–CoAl-LDHs have been prepared using an *in situ* redox process (Scheme 1) [7,10]. Ag–CoAl-LDHs have been prepared by dispersing CoAl-LDHs in a $AgNO_3$ aqueous solution. During the preparation, the abundant surface hydroxyl groups of CoAl-LDHs can react with Ag^+ ions to afford Ag_2O. Under indoor light, Ag_2O undergoes a self-redox reaction to form Ag NPs on the surface of CoAl-LDHs [10]. Pt–CoAl-LDHs and Pd–CoAl-LDHs have been prepared by mixing CoAl-LDHs with a Na_2PtCl_4 or Na_2PdCl_4 aqueous solution. Due to the reductive nature of Co^{2+} in the CoAl-LDHs and the oxidative nature of $PtCl_4^{2-}$ or $PdCl_4^{2-}$, Pt^{2+} or Pd^{2+} is reduced to Pt^0 or Pd^0, which is then nucleated and further grown into Pt or Pd NPs on the surface of CoAl-LDHs [7]. The XRD patterns of all of the N–CoAl-LDHs exhibit the specific diffraction peaks of CoAl-LDHs (Fig. S1). The specific surface area of Ag–CoAl-LDHs (346.9 m^2/g), Pt–CoAl-LDHs (29.9 m^2/g) and Pd–CoAl-LDHs (42.8 m^2/g) are larger than that of CoAl-LDHs (18.5 m^2/g), which is due to the immobilization of the noble metal NPs on the LDH layers (Fig. S2). It should be noted that the specific surface area of Ag–CoAl-LDHs is significant different from other N–CoAl-LDHs because the large amounts of deposited Ag NPs have formed the pile hole [11]. The Co 2p and Al 2p XPS spectra of CoAl-LDHs and N-CoAl-LDHs exhibit nearly the same binding energy for the Co $2p_{5/2}$, Co $2p_{3/2}$ and Al 2p peaks, which confirms that the structure of the LDHs remains unchanged after immobilization of the noble

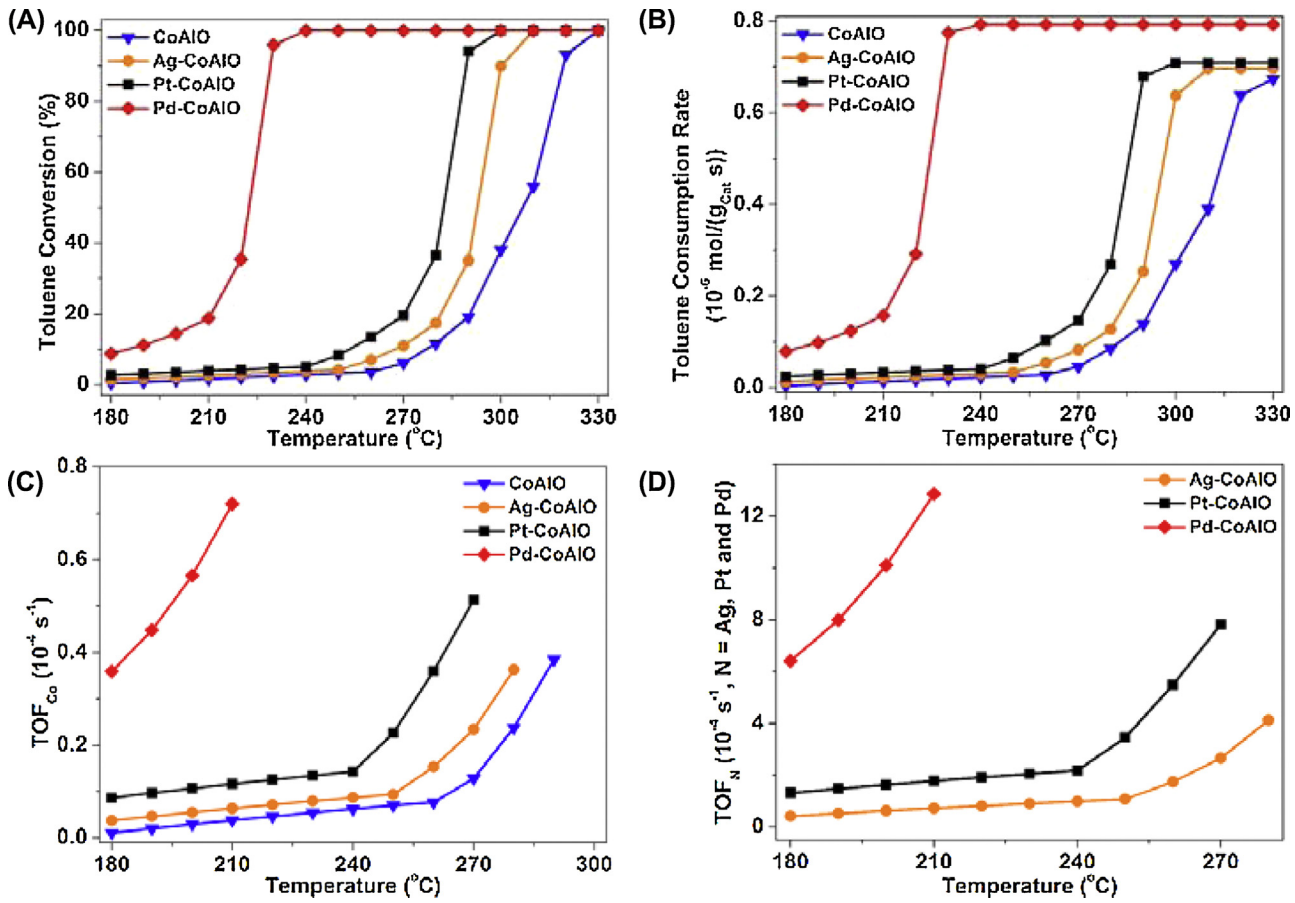

Fig. 1. Toluene conversion (A), toluene consumption rate (B), TOF_{Co} (C) and TOF_N (D) as a function of temperature over the CoAlO and N–CoAlO catalysts. Reaction conditions: 0.10 g catalyst, 2000 ppm toluene, 20% O_2, balance N_2, total flow rate = 100 ml/min, GHSV = 60,000 ml/(g h).

metal NPs (Figs. S3A and B). In addition, the Ag 3d XPS spectra of Ag–CoAl-LDHs contained Ag $3d_{5/2}$ and Ag $3d_{3/2}$ peaks at binding energies of 368.0 and 374.1 eV, indicating only the presence of Ag^0 (Fig. S3C). The Pt 4f XPS spectrum of Pt–CoAl-LDHs exhibits two XPS peaks corresponding to Pt $4f_{5/2}$ and Pt $4f_{7/2}$, which are centered at 78.1 and 74.4 eV, respectively (Fig. S3D). These results demonstrate that ~92% of the platinum is in the metallic form (Pt^0). Similarly, ~89% of the palladium in Pd–CoAl-LDHs (Fig. S3E) is in the metallic form (Pd^0). The thermogravimetric analysis (TGA) curve for CoAl-LDHs is shown in Fig. S4A. Two weight loss stages were observed as the temperature increased from 50 to 800 °C. The first weight loss of 12.42% occurred between 30 and 202 °C due to the removal of water molecules (Calcd. $0.71H_2O$ per CoAl-LDH). The second weight loss step of 17.31% at 202–756 °C was due to the collapse of the layered structure. A similar explanation can be applied to the TGA results of Ag–CoAl-LDHs, Pt–CoAl-LDHs and Pd–CoAl-LDHs (Figs. S4B–D). Based on the TGA and ICP analyses, the molecular formulas of CoAl-LDHs and N–CoAl-LDHs were determined to be $Co_{0.66}Al_{0.34}(OH)_2(CO_3)_{0.17}\cdot 0.71H_2O$, $Ag_{0.096}Co_{0.66}Al_{0.34}(OH)_2(CO_3)_{0.17}\cdot 0.72H_2O$, $Pt_{0.018}Co_{0.66}Al_{0.34}(OH)_2(CO_3)_{0.17}\cdot 0.38H_2O$ and $Pd_{0.034}Co_{0.66}Al_{0.34}(OH)_2(CO_3)_{0.17}\cdot 0.68H_2O$. The ICP results for N–CoAl-LDHs indicated Ag, Pt and Pd weight percentages of 8.96%, 3.42% and 3.35%, respectively. The TEM images of N–CoAl-LDHs confirm the presence of noble metal NPs on the surface of the CoAl-LDH layers, and the majority of the Ag, Pt and Pd NPs are in the range of 10.5, 21.2 and 22.7 nm, respectively (Figs. S5 and S6). Therefore, these characterizations indicate that the noble metal NPs were successfully immobilized on the CoAl-LDHs *via* the *in situ* redox process. The CoAl-LDHs not only serve as a support for the noble metal NPs but also participate in the reduction reaction. In addition, the CoAl-LDH and N–CoAl-LDH precursors are calcined in air at 600 °C to afford the corresponding CoAlO, Ag–CoAlO, Pt–CoAlO and Pd–CoAlO catalysts for toluene combustion.

3.2. Catalytic combustion performance of CoAlO and N–CoAlO

The combustion of toluene has been studied over the CoAlO and N-CoAlO catalysts in a temperature range of 180–330 °C under 2000 ppm toluene + 20% O_2 + balance N_2 with a total flow rate of 100 ml/min, which affords 60,000 ml/(g h) over 0.10 g of catalyst. Fig. 1 shows the catalytic activities of the various catalysts. The toluene conversion and toluene consumption rate increased as the temperature increased (Fig. 1A and B). For convenience, the catalytic activity of the catalysts was compared using the T_{10}, T_{50} and T_{90} reaction temperatures (corresponding to toluene conversion = 10%, 50% and 90%, respectively), as summarized in Table 1. These results suggest that the catalytic activity increased in the following order: CoAlO < Ag–CoAlO < Pt–CoAlO < Pd–CoAlO. It important to note that toluene has been completely oxidized to CO_2 and H_2O over these catalysts, and no other incomplete oxidation products were detected in the catalytic system, which was confirmed by a carbon balance of 99.5% in each run.

Fig. 1C and D shows the dependence of the TOF_{Co} and TOF_N (N = Ag, Pt and Pd) on the reaction temperature in the catalytic combustion of toluene at a conversion less than 20% over the

Table 1
Reaction temperature, TOF_{Co}, TOF_N and activation energy (E_a) of the CoAlO and N–CoAlO catalysts for toluene combustion.

Catalyst	T_{10} (°C)	T_{50}(°C)	T_{90}(°C)	TOF_{Co} at 210 °C(10^{-4} s^{-1})	TOF_N at 210 °C(10^{-4} s^{-1})[a]	E_a (kJ/mol)
CoAlO	277	307	319	0.038	–	147.5
Ag–CoAlO	267	293	300	0.064	0.723	117.9
Pt–CoAlO	254	282	289	0.116	1.775	110.3
Pd–CoAlO	185	222	226	0.721	12.864	49.5

[a] N: Ag, Pt or Pd.

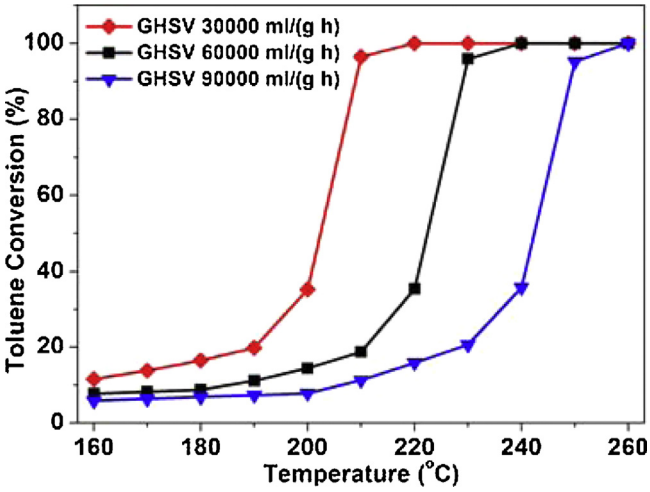

Fig. 2. Effect of GHSV on the catalytic activity over Pd–CoAlO. Reaction conditions: 0.10 g Pd–CoAlO, 2000 ppm toluene, 20% O_2, balance N_2.

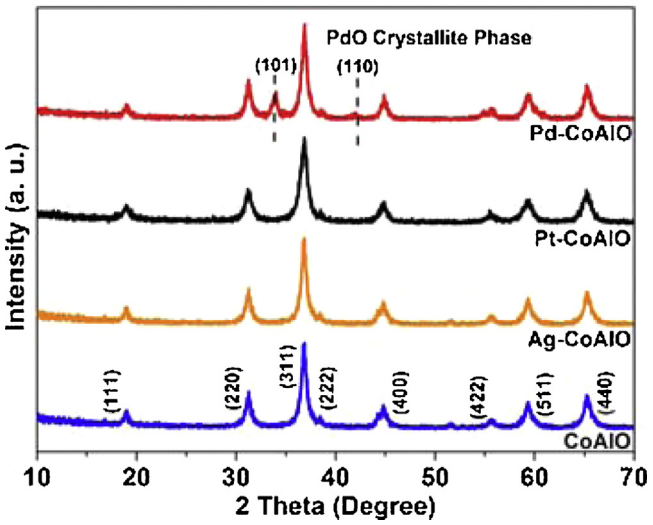

Fig. 3. XRD patterns for CoAlO and N–CoAlO.

CoAlO and N–CoAlO catalysts. The TOF values over each catalyst increased as the reaction temperature increased. The changing trends in the TOF as a function of reaction temperature over different catalysts are similar to those observed for toluene conversion as a function of reaction temperature. The TOF_{Co} values confirm that the catalytic activity increased in the following order: CoAlO < Ag–CoAlO < Pt–CoAlO < Pd–CoAlO. It is important to note that the catalytic activity of Pd–CoAlO is much better than that of Pt–CoAlO, which is consistent with previously reported results for Pd/Al_2O_3 and Pt/Al_2O_3 [12]. Therefore, these results indicate that the Pd–CoAlO catalysts exhibit the best catalytic activity with the lowest reaction temperature and highest TOF values.

Fig. 2 shows the catalytic activity of Pd–CoAlO at different GHSVs. At the same temperature, the toluene conversion decreased as the GHSV increased. This result indicates that a longer contact time is beneficial for improving the catalytic activity. It is important to note that under similar reaction conditions over the LDH-derived spinel oxides (Table S6), the catalytic activity (T_{90} = 226 °C) over the Pd–CoAlO catalyst is better than those (T_{90} = 230 °C) over Pd/Co_3AlO(COP) [4b], (T_{90} = 250 °C) over $Co_2Mn_4Al_2O$-450 [13a], (T_{90} = 258 °C) over CoMn(0.5)AlO [13b], (T_{90} = 261 °C) over Mn_6Al_2O [13c], (T_{90} = 286 °C) over Ce(E)/CoMgAlO [13d], (T_{90} = 290 °C) over MgMnAlO(COP) [13e], (T_{90} = 300 °C) over Cu_4Al_2O [13f], (T_{90} = 307 °C) over MnCuAlO-450 [13g] and (T_{90} = 310 °C) over CoMgAlO [13h] but inferior to that (T_{90} = 145 °C) over 0.9 wt.% K/Co_4MnAlO [13i]. Nevertheless, the catalytic activity (T_{90} = 226 °C) over the Pd–CoAlO catalyst is better than those (T_{90} = 260 °C) over 1.0 wt.% Pt/Al_2O_3 [14] and (T_{90} = 230 °C) over Pd–Au/TiO_2 [5d]. Therefore, the relatively lower reaction temperature among the reported catalysts makes Pd–CoAlO a promising catalyst for toluene combustion.

These catalytic results indicate that the Pd–CoAlO catalysts exhibit the best catalytic activity with the lowest reaction temperature and highest TOF values among the CoAlO and N–CoAlO catalysts. In addition, the relatively lower reaction temperature among the reported catalysts makes Pd–CoAlO a promising catalyst for toluene combustion. Therefore, further characterization is required to investigate the relationship between the structure and catalytic activity of the CoAlO and N–CoAlO catalysts.

3.3. Characterization of CoAlO and N–CoAlO

The XRD patterns of CoAlO and N–CoAlO are shown in Fig. 3. The LDH precursors were completely transformed to spinel oxide phases. For CoAlO, diffraction peaks located at 18.9°, 31.3°, 36.8°, 38.5°, 44.8°, 55.7°, 59.4° and 65.2° were observed, corresponding to the (1 1 1), (2 2 0), (3 1 1), (2 2 2), (4 0 0), (4 2 2), (5 1 1), and (4 4 0) planes, respectively, of the spinel oxide phases (Co_2AlO_4, JCPDS 38-0814; $CoAl_2O_4$, JCPDS 44-0160 and 82-2246; Co_3O_4, JCPDS 74-2120) [15]. It is important to note that the two diffraction peaks located at 2θ = 33.9° and 42.2° were observed in the XRD pattern of Pd–CoAlO. These two diffraction peaks are assigned to (1 0 1) and (1 1 0) of PdO. Previous results indicated that the PdO formed on the surface of Pd NPs during calcination of Pd–CoAl-LDHs in air is more active than metallic Pd in VOC combustion [5a,5b]. The XRD results reveal that (1) the CoAl-LDH and N–CoAl-LDH precursors were transformed to CoAlO and N–CoAlO spinel oxide phases and (2) the XRD pattern of Pd–CoAlO indicated the existence of catalytically active PdO, which contributes to the excellent catalytic activity of the Pd–CoAlO catalyst in toluene combustion.

The Raman spectra of the CoAlO and N–CoAlO catalysts are shown in Fig. 4. The CoAlO catalyst exhibited five peaks located at 199, 486, 524, 617 and 688 cm^{-1}, which correspond to the $F_{2g}^{(1)}$, E_g, $F_{2g}^{(2)}$, $F_{2g}^{(3)}$ and A_{1g} symmetries, respectively, of CoAlO [16]. The A_{1g} Raman peaks of CoAlO and N–CoAlO increase in the following order: Pd–CoAlO (668 cm^{-1}) < Pt–CoAlO (672 cm^{-1}) < Ag–CoAlO (677 cm^{-1}) < CoAlO (688 cm^{-1}). In comparison to the A_{1g} Raman peaks of CoAlO, the A_{1g} Raman peaks of N–CoAlO exhibit a red shift. The Raman results indicate that (1) the red-shift of the Raman peaks is consistent with the catalytic activity order of the cata-

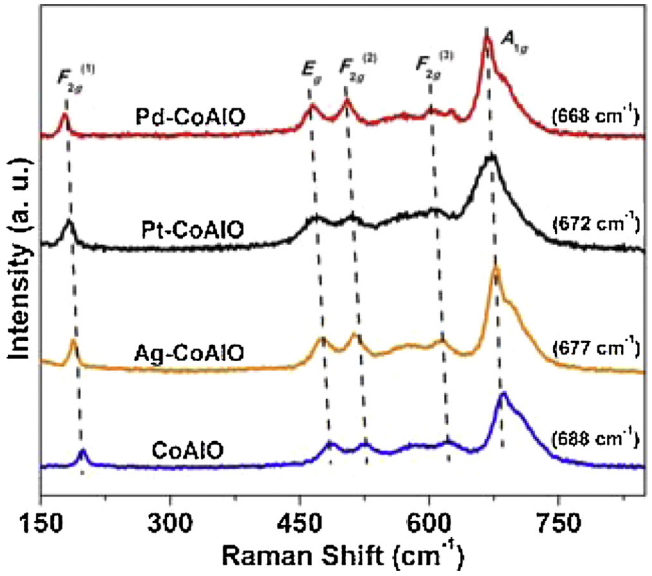

Fig. 4. Raman spectra of CoAlO and N–CoAlO. (For interpretation of the references to color in the text, the reader is referred to the web version of this article.)

lysts and (2) the immobilization of noble metal NPs leads to a more substantial red shift compared to that of CoAlO. The red shift indicates that N–CoAlO causes lattice distortion or residual stress in the spinel structure. The existence of lattice defects is beneficial for the formation of oxygen vacancies, which can activate, adsorb oxygen gas, and provide lattice sites for oxygen migration [17]. Therefore, Pd–CoAlO tends to form the most oxygen vacancies because it has the largest red shift (20 cm^{-1}) compared to CoAlO. The Raman spectra of the above catalysts show clear red-shifts, which indicate the incorporation of noble metal ions in the spinel matrix. The lattice parameter (*a*) in Table 2 have confirm the above results as the lattice parameter (*a*) of N–CoAlO are all larger than that of CoAlO [3c]. In addition, the Raman spectra of Al_2O_3, Co_3O_4, CoAlO and N–CoAlO have been compared (Fig. S7). These results indicate that (1) no characteristic Al_2O_3 peaks were observed in the Raman spectra of CoAlO and N-CoAlO, which no Al_2O_3 phase was formed during the calcination of CoAl-LDHs and N-CoAl-LDHs. (2) In addition, CoAlO and N–CoAlO have similar peaks corresponding to Co_3O_4 oxides, confirming that the obtained CoAlO and N–CoAlO exist in pure spinel oxide phases. These results confirm that the transformation of pure spinel oxide phases (*i.e.*, Co_2AlO_4 and $CoAl_2O_4$) without the formation of the Al_2O_3 phase during the calcination of CoAl-LDHs and N–CoAl-LDHs in air at 600 °C.

The nitrogen adsorption–desorption isotherms and pore size distribution patterns for CoAlO and N–CoAlO are shown in Fig. 5. The isotherms for CoAlO and N-CoAlO are consistent with type IV isotherms with a larger hysteresis compared to the corresponding LDH precursors [18], which indicates improved mesoporosity. The improved mesoporosity can overcome the diffusional limitation problems and improves the accessibility of the active sites to the reagent molecules [19]. The surface area, pore volume and pore diameter of CoAlO and N–CoAlO are shown in Table 2. In Table 2, the values for N–CoAlO are quite different from those for CoAlO, which indicates that immobilization of noble metal NPs on CoAlO leads to changes in the surface properties of CoAlO. To explain the relationship between the structure and catalytic activity of CoAlO and N–CoAlO, additional characterization, such as TEM, H_2-TPR and XPS, is required.

As shown in Fig. 6 and Fig. S8, all of the CoAlO and N–CoAlO catalysts consist of hexagonal nanosheets, and the average size of these nanosheets is 3 μm. The CoAlO catalysts exhibit surface lattice spacings of 0.286 and 0.467 nm, which correspond to the (2 2 0) and (1 1 1) crystal planes, respectively (Fig. S8). The immobilization of noble metal NPs (Ag, Pt and Pd) results in black spots (Fig. 6A, E and I) that correspond to uniformly distributed noble metal NPs on the surface of the hexagonal nanosheets. All of the N–CoAlO catalysts possess (2 2 0) and (1 1 1) faces of CoAlO (Figs. 6B, F and J), and Ag–CoAlO and Pt–CoAlO possess Ag (1 1 1) and Pt (1 1 1) crystal planes with a lattice spacing of 0.236 and 0.227 nm, respectively (Figs. 6C and G). It is important to note that Pd–CoAlO possesses the PdO (1 0 1) crystal plane with a lattice spacing of 0.264 nm (Fig. 6K). These TEM results confirm the XRD results for Pd–CoAlO, in which the (1 0 1) diffraction peak of catalytically active PdO [5a,5b] was observed. The particle size distribution of the noble metal NPs on N–CoAlO (Fig. 6D, H and L) indicates that the average particle size of the noble metal NPs decreased in the following order: Ag–CoAlO (87.8 nm) > Pt-CoAlO (52.1 nm) > Pd–CoAlO (39.3 nm). In combination with the catalytic results of N-CoAlO, Pd–CoAlO, which has a relatively small Pd NP size of 39.3 nm, exhibits the highest catalytic activity, and Ag–CoAlO and Pt–CoAlO, which have larger Ag and Pt NP sizes (87.8 and 52.1 nm), exhibit lower catalytic activity compared to Pd–CoAlO. Therefore, the noble metal NP sizes of N–CoAlO affected the catalytic activity of toluene combustion. As shown in Fig, noble metal NP sizes are quite large (40–80 nm) due to the bad dispersion of noble metal precursors (*i.e.*, $AgNO_3$, Na_2PtCl_4 and Na_2PdCl_4) and the relative fast ramping rate during the preparation of N–CoAlO. As such, more work such as the addition of dispersing agent (*i.e.*, PVP or PVA) and the reduction of the ramping rate should be done in the near future to reduce the sizes of noble metal NP [20]. The TEM results indicate that (1) all of the CoAlO and N–CoAlO catalysts consist of hexagonal nanosheets with (2 2 0) and (1 1 1) crystal planes and (2) the noble metal NPs, which have characteristic crystal planes, were uniformly distributed on the surface of the CoAlO nanosheets. In addition, the noble metal NP sizes of N–CoAlO decreased in the following order: Ag–CoAlO > Pt–CoAlO > Pd–CoAlO. Therefore, the noble metal NP sizes of N–CoAlO affected the catalytic activity of toluene combustion, and the existence of catalytically active PdO contributes to the excellent catalytic activity of Pd–CoAlO in toluene combustion.

H_2-TPR experiments were performed to investigate the reducibility of CoAlO and N–CoAlO. As shown in Fig. 7A, the CoAlO catalyst exhibited three peaks. The first two peaks correspond to the reduction of Co^{3+} to Co^{2+}, and the last peak was due to the reduction of Co^{2+} to Co^0 [19]. After immobilization of noble metal NPs on CoAlO, the first two reduction peaks of N–CoAlO merge to form one reduction peak, and all of the reduction peaks shift to lower temperatures, indicating the presence of a strong interaction between the noble metal NPs and the CoAlO support. The strong

Table 2
Lattice parameters and porous structure parameter of CoAlO and N–CoAlO.

Catalyst	Crystal system	*a* (Å)	Surface area (m^2/g)	Pore volume (cm^3/g)	Pore diameter (nm)
CoAlO	Cubic	8.09	88.6	0.229	5.6
Ag–CoAlO	Cubic	8.13	69.5	0.240	6.5
Pt–CoAlO	Cubic	8.16	81.1	0.240	6.5
Pd–CoAlO	Cubic	8.18	51.8	0.247	7.8

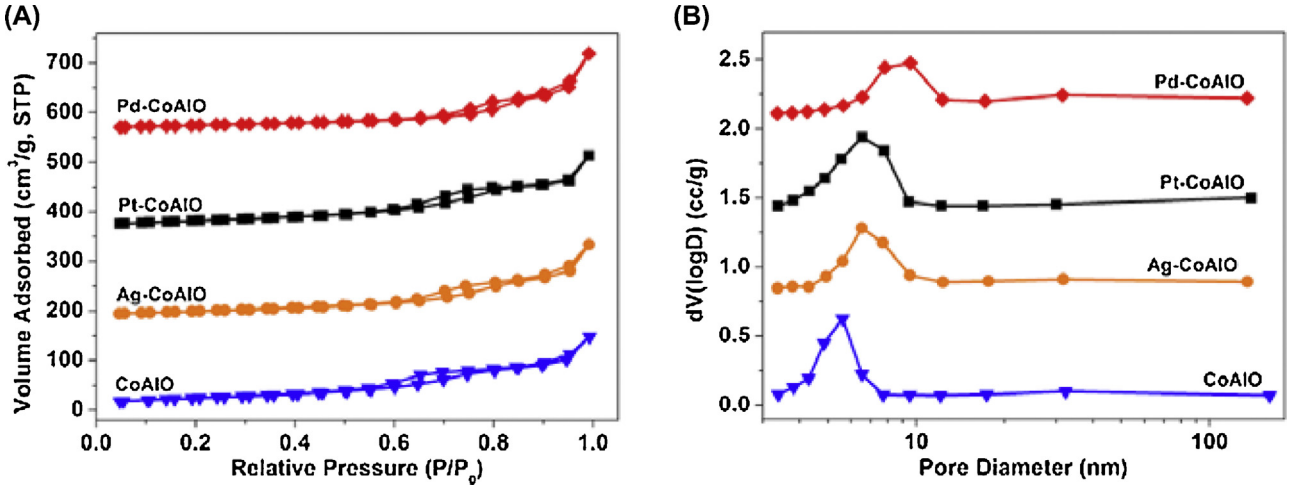

Fig. 5. Adsorption–desorption isotherms (A) and pore size distribution curves (B) for CoAlO and N–CoAlO.

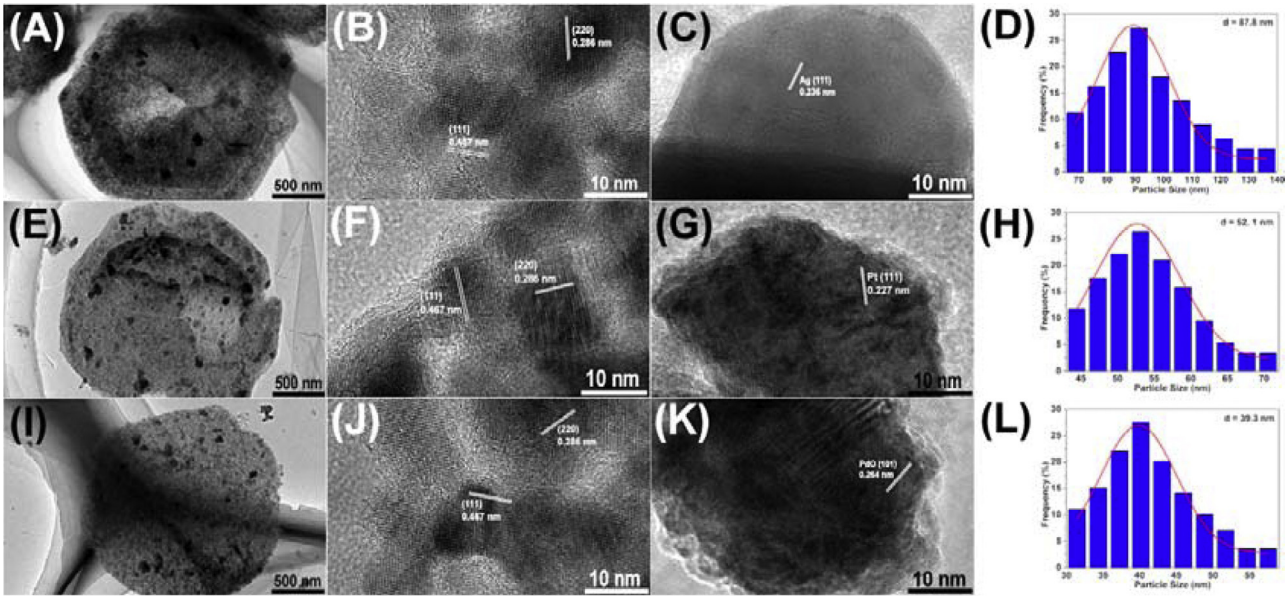

Fig. 6. TEM results for Ag-CoAlO (A–D), Pt-CoAlO (E–H) and Pd–CoAlO (I–L).

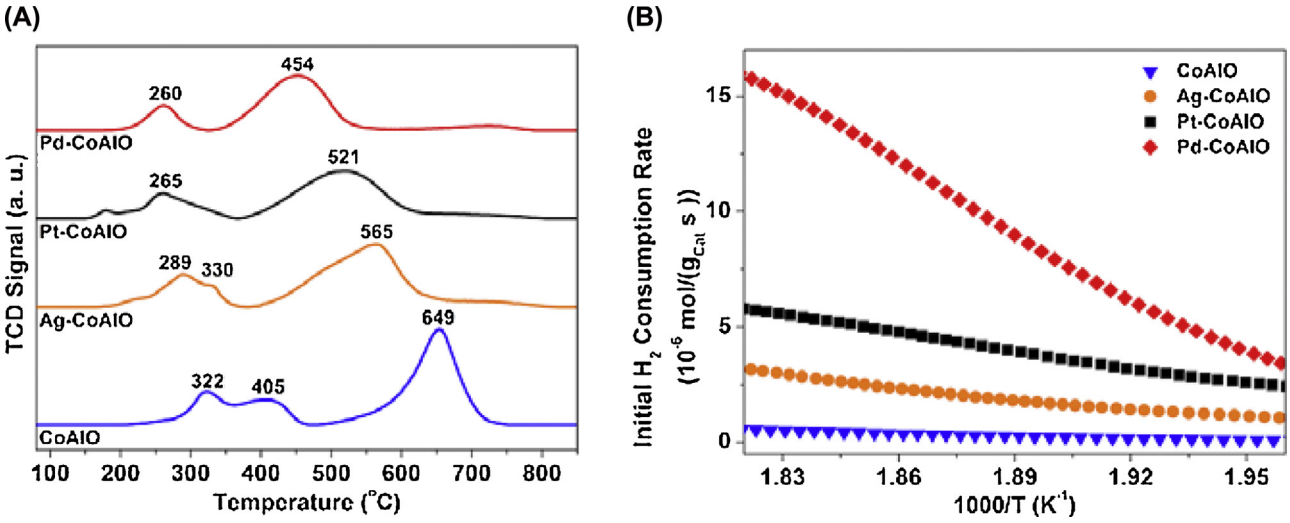

Fig. 7. H_2-TPR spectra (A) and initial H_2 consumption rate (B) of CoAlO and N–CoAlO.

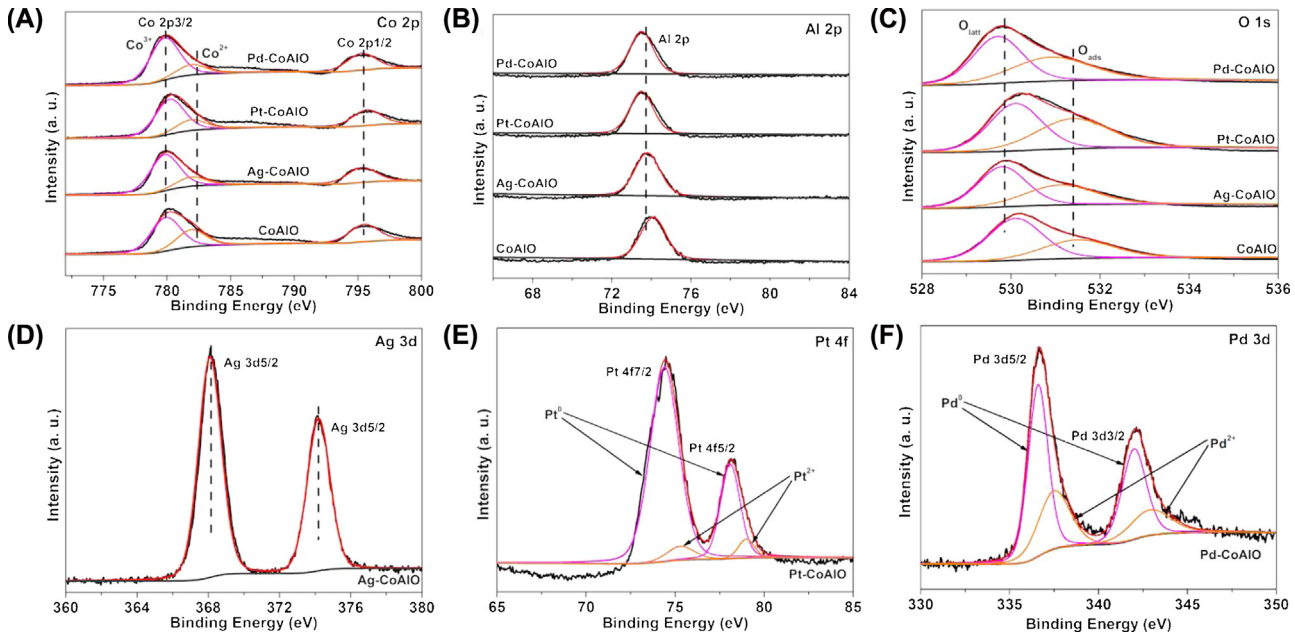

Fig. 8. XPS spectra of CoAlO and N–CoAlO.

Table 3
H_2 consumption and surface elemental composition of CoAlO and N–CoAlO.

Catalyst	Surface element molar ratio				H_2 consumption (mmol/g)		
	N/Co[a]	N^{2+}/N^{0}[b]	Co^{3+}/Co^{2+}	O_{ads}/O_{latt}	Peak 1 + 2	Peak 3	Total
CoAlO	–	–	1.97	0.52	3.18	6.39	9.57
Ag–CoAlO	0.13	–	3.88	0.72	2.28	7.08	9.36
Pt–CoAlO	0.06	0.15	3.97	0.80	1.71	5.28	6.99
Pd–CoAlO	0.06	0.52	4.15	0.90	1.01	4.55	5.56

[a] N: Ag, Pt or Pd.
[b] N^{2+}/N^{0}: Pt^{2+}/Pt^{0} or Pd^{2+}/Pd^{0}.

interaction improves the low temperature reducibility of N–CoAlO. This improvement will be beneficial for enhancing the catalytic performance because VOC combustion proceeds *via* a Mars-van Krevelen (redox) mechanism [21]. It is better to use the initial (when less than 25% of the oxygen in the samples has been consumed for the first reduction peak) H_2 consumption rate to evaluate the low temperature reducibility of the catalysts [22]. The results in Fig. 7B indicate that the low temperature reducibility increased in the following order: CoAlO < Ag–CoAlO < Pt–CoAlO < Pd–CoAlO. The H_2-TPR results indicate that (1) the low temperature reducibility order of the catalysts is consistent with the catalytic activity order of the catalysts. (2) In addition, the Raman results indicate that the deposition of noble metal NPs results in the formation of more oxygen vacancies in the N–CoAlO catalysts compared to that formed in CoAlO, enhancing the low temperature reducibility. In addition, XPS characterization has been carried out to investigate the sur-

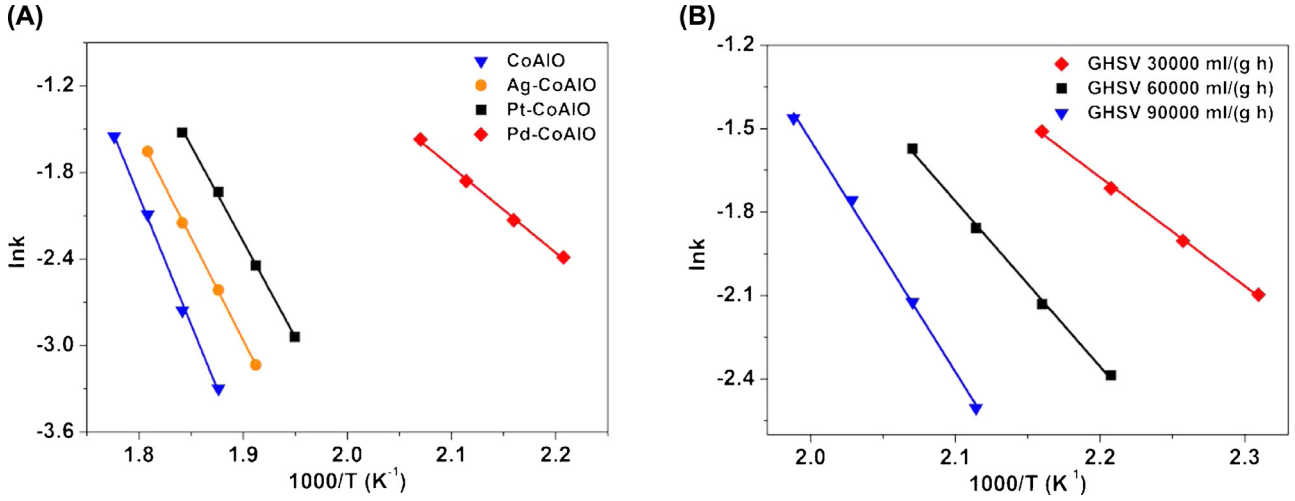

Fig. 9. Arrhenius plots for toluene combustion over CoAlO and N–CoAlO.

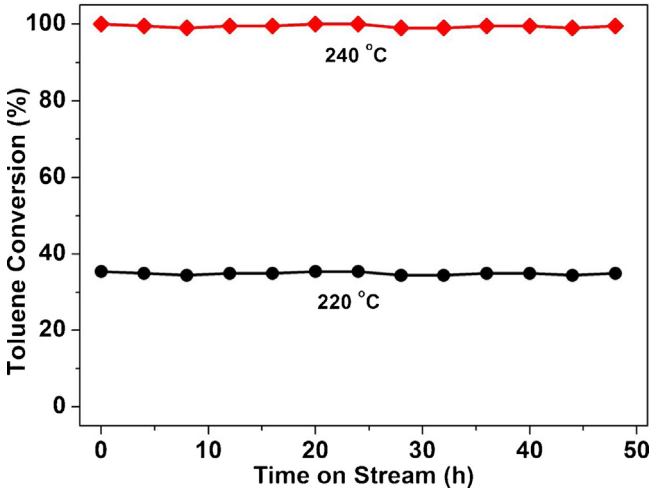

Fig. 10. Toluene combustion as a function of time on stream over Pd–CoAlO. Reaction conditions: 0.10 g catalyst, 2000 ppm toluene, 20% O_2, balance N_2, total flow rate = 100 ml/min, GHSV = 60,000 ml/(g h).

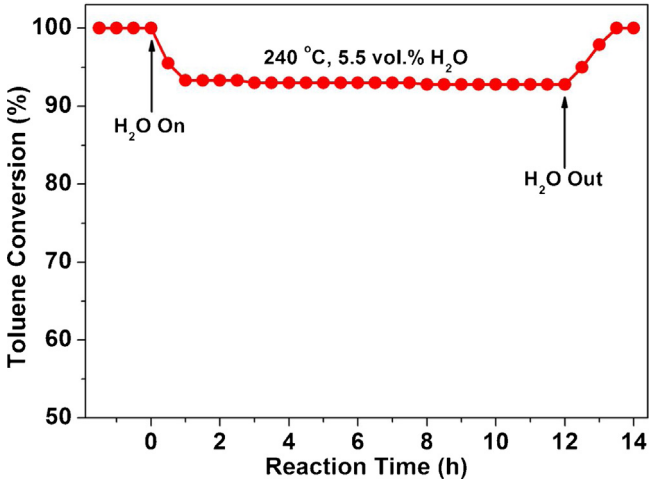

Fig. 11. Effect of 5.5 vol.% H_2O on toluene combustion over Pd–CoAlO at 240 °C. Reaction conditions: 0.10 g catalyst, 2000 ppm toluene, 5.5 vol.% H_2O, 20% O_2, balance N_2, total flow rate = 100 ml/min, GHSV = 60,000 ml/(g h).

face composition, metal oxidation state, and oxygen species of the CoAlO and N–CoAlO catalysts.

Fig. 8 shows the Co 2p, Al 2p, O 1s, Ag 3d, Pt 4f and Pd 3d XPS spectra of the CoAlO and N–CoAlO catalysts. As shown in Fig. 8A, the asymmetrical Co $2p_{3/2}$ XPS spectrum of each catalyst can be decomposed into two components at binding energies of 780.1 and 781.9 eV, which correspond to surface Co^{3+} and Co^{2+} species, respectively [4d]. As summarized in Table 3, the surface Co^{3+}/Co^{2+} molar ratio increased in the following order: CoAlO (1.97) < Ag–CoAlO (3.88) < Pt–CoAlO (3.97) < Pd–CoAlO (4.15). The Al 2p XPS spectrum of the catalysts remains unchanged after immobilization of the noble metal NPs, which indicates that the major structure of N–CoAlO remains untouched after immobilization (Fig. 8B). The results in Fig. 8C indicate that O 1s exhibits signals at binding energies of 529.9 and 531.1 eV, which correspond to surface lattice oxygen (O_{latt}) species and surface adsorbed oxygen (O_{ads}) [23]. As shown in Table 3, the surface O_{ads}/O_{latt} molar ratio increased in the following order: CoAlO (0.52) < Ag–CoAlO (0.72) < Pt–CoAlO (0.80) < Pd–CoAlO (0.90). As shown in Fig. 8D, Ag 3d contains a signal at a binding energy of 368.1 eV, which corresponds to the presence of Ag^0 in Ag–CoAlO [24]. The Pt 4f XPS spectrum of Pt–CoAlO (Fig. 8E) contains two XPS peaks consisting of Pt $4f_{5/2}$ and Pt $4f_{7/2}$, which are centered at 78.1 and 74.4 eV, respectively. These results indicate that ~87% of the platinum is in the metallic form (Pt^0). As shown in Fig. 8F, the Pd 3d XPS spectrum of Pd–CoAlO indicates that ~66% of the palladium is the metallic form (Pd^0) based on Pd $3d_{3/2}$ and Pd $3d_{5/2}$, which are centered at 342.0 and 336.6 eV, respectively. The XPS results indicate that (1) the surface Co^{3+}/Co^{2+} molar ratio order of the catalysts is consistent with the catalytic activity order of the catalysts, which indicates that the deposition of noble metal NPs increased the Co^{3+} ions and decreased the Co^{2+} ions. (2) In addition, the surface O_{ads}/O_{latt} molar ratio order of the catalysts is consistent with the catalytic activity order of the catalysts, indicating that the N–CoAlO catalysts have more abundant O^{2-} species than CoAlO due to the presence of noble metal NPs in the top layer, and 3) all of the Ag NPs in Ag–CoAlO are in the metallic state (*i.e.*, ~87% of the Pt NPs in Pt–CoAlO are in the metallic state and ~66% of the Pd NPs in Pd–CoAlO are in the metallic state. These XPS results are consistent with the XRD and TEM results for Pd–CoAlO, and catalytically active PdO was observed. Based on previous results, PdO is more active than metallic Pd in VOC combustion [5a,5b]. In combination with the catalytic results in Table 1 and the above characterization results, the catalytic performance of the catalysts is associated with low temperature reducibility and surface Co^{3+} and O_{ads} species. The Pd–CoAlO catalyst exhibits the highest catalytic activity because it has the highest low temperature reducibility and the most abundant surface Co^{3+} and O_{ads} species. In addition, the noble metal NP sizes of N–CoAlO affected the catalytic activity in toluene combustion, and the existence of catalytically active PdO contributes to the excellent catalytic activity of Pd–CoAlO for toluene combustion.

3.4. Kinetic parameters

A dimensionless Weisz–Prater parameter of less than 0.3 with an effectiveness factor higher than 0.95 and reaction order of 1 provide sufficient conditions for overcoming the significant pore diffusion limitations [25]. At a toluene conversion <20%, a Weisz-Prater analysis was performed, and the calculated Weisz–Prater criterion (N_{W-P}) values in our catalytic systems are much less than 0.3. Therefore, no significant mass transfer limitations existed in our catalytic systems. The catalytic combustion of toluene in the presence of excess oxygen follows first-order and zero-order kinetics with respect to the toluene concentration and oxygen concentration, respectively [26]. Therefore, it is reasonable to assume that the toluene combustion in the presence of excessive oxygen should obey first-order kinetics, and the equation is as follows:

$$r = -kc = \left[-A\exp\left(-\frac{E_a}{RT}\right)\right]c \quad (4)$$

where r, k, A, and E_a re the reaction rate (μmol/(g s)), rate constant (s^{-1}), pre-exponential factor, and apparent activation energy (kJ/mol), respectively. The k values can be calculated from the reaction rates and reactant conversions.

Fig. 9A shows the Arrhenius plots for the catalytic combustion of toluene at a conversion less than 20% over the CoAlO and N–CoAlO catalysts. The linearity of these plots indicates that the reaction only remains in the kinetically controlled region at low temperatures where the conversion is less than 20%, which is in good agreement with previous results [4f]. Based on the slopes of the Arrhenius plots, the apparent activation energies (E_a) have been calculated and are summarized in Table 1. The results indicate that the E_a values decreased in the following order: CoAlO (147.5 kJ/mol) > Ag–CoAlO (117.9 kJ/mol) > Pt–CoAlO (110.3 kJ/mol) > Pd–CoAlO (49.5 kJ/mol). The lowest E_a value for Pd–CoAlO confirms that the Pd–CoAlO catalyst exhibits the best catalytic activity for toluene combustion. The results in Fig. 9B indicate that the E_a values for Pd–CoAlO at different GHSVs decreased in

the following order: 90,000 ml/(g h) (69.2 kJ/mol) > 65,000 ml/(g h) (49.5 kJ/mol) > 30,000 ml/(g h) (32.5 kJ/mol). The lowest E_a value was observed at GHSV = 30,000 ml/(g h), which confirms that a longer contact time is beneficial for improving the catalytic activity.

3.5. Stability of the catalyst

To examine the catalytic stability, lifetime experiments were carried out over Pd–CoAlO within 48 h of on-stream reaction at different temperatures (220 and 240 °C). As shown in Fig. 10, no significant decrease in the catalytic activity was observed during the 48 h on stream at these temperatures. The XRD patterns of the fresh and used Pd–CoAlO catalysts contain the same diffraction peaks (Fig. S9A), and the Raman spectra of the fresh and used Pd–CoAlO catalysts exhibit the same characteristic peaks (Fig. S9B). The TEM results of the used Pd–CoAlO catalyst (Fig. S10) indicated that the hexagonal nanosheet morphology was retained and the average Pd NP size (48.3 nm) was slightly larger than that of the fresh Pd–CoAlO catalyst (39.3 nm). These results indicate that Pd–CoAlO is catalytically stable. In addition, the structure of the Pd–CoAlO catalyst remains unchanged after the reaction.

3.6. Effect of water

Because water vapor in toluene combustion often leads to deactivation of the catalyst, the catalytic activity of Pd–CoAlO in the presence of water vapor needs to be considered. As shown in Fig. 11, when 5.5 vol.% H_2O was introduced to the stream at 240 °C, the toluene conversion decreased slightly but remained higher than 92% during the activity test for 12 h. This result indicates that water vapor inhibits the slightly catalytic activity at 240 °C due to the competitive adsorption of water and toluene molecules on the active sites [3c]. After the water vapor was removed, the toluene conversion at 240 °C nearly recovered. These results suggest that the Pd–CoAlO catalyst can tolerate the presence of water vapor and maintain excellent catalytic activity to a certain extent.

3.7. Comparison experiments

The comparison of catalytic activities between MgAlO, CoAlO, Pd-MgAlO and Pd–CoAlO has been carried out to investigate the role of cobalt in the studied catalytic system (Fig 12). It should be noted that the preparation of the precursor Pd–MgAl–LDHs is

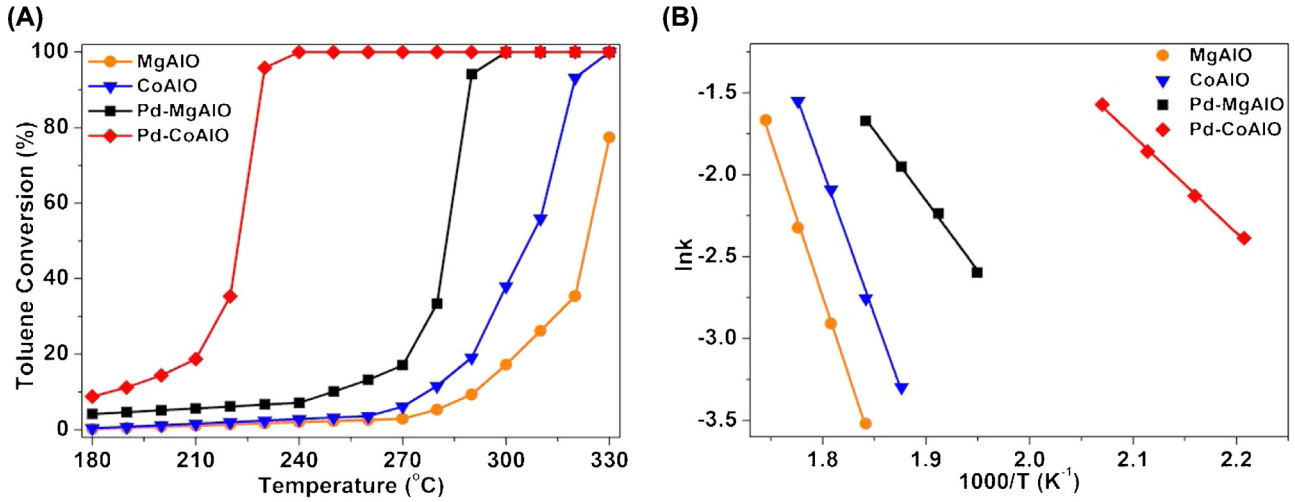

Fig. 12. Toluene conversion (A) and Arrhenius plots (B) for toluene combustion over MgAlO, CoAlO, Pd–MgAlO and Pd–CoAlO. Reaction conditions: 0.10 g catalyst, 2000 ppm toluene, 20% O_2, balance N_2, total flow rate = 100 ml/min, GHSV = 60,000 ml/(g h).

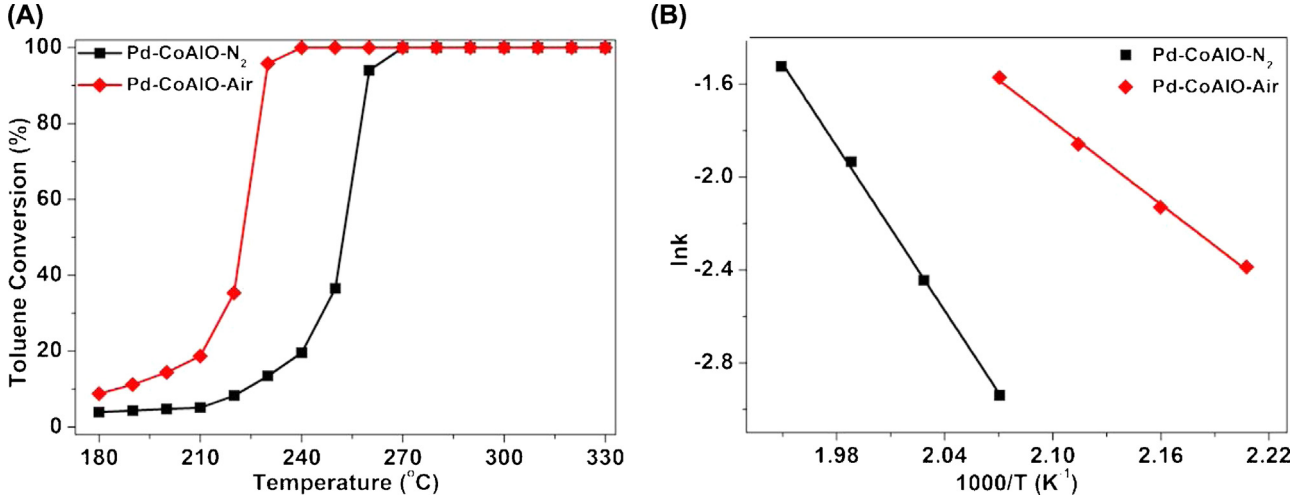

Fig. 13. Toluene conversion (A) and Arrhenius plots (B) for toluene combustion over Pd–CoAlO–N_2 and Pd–CoAlO–Air. Reaction conditions: 0.10 g catalyst, 2000 ppm toluene, 20% O_2, balance N_2, total flow rate = 100 ml/min, GHSV = 60,000 ml/(g h).

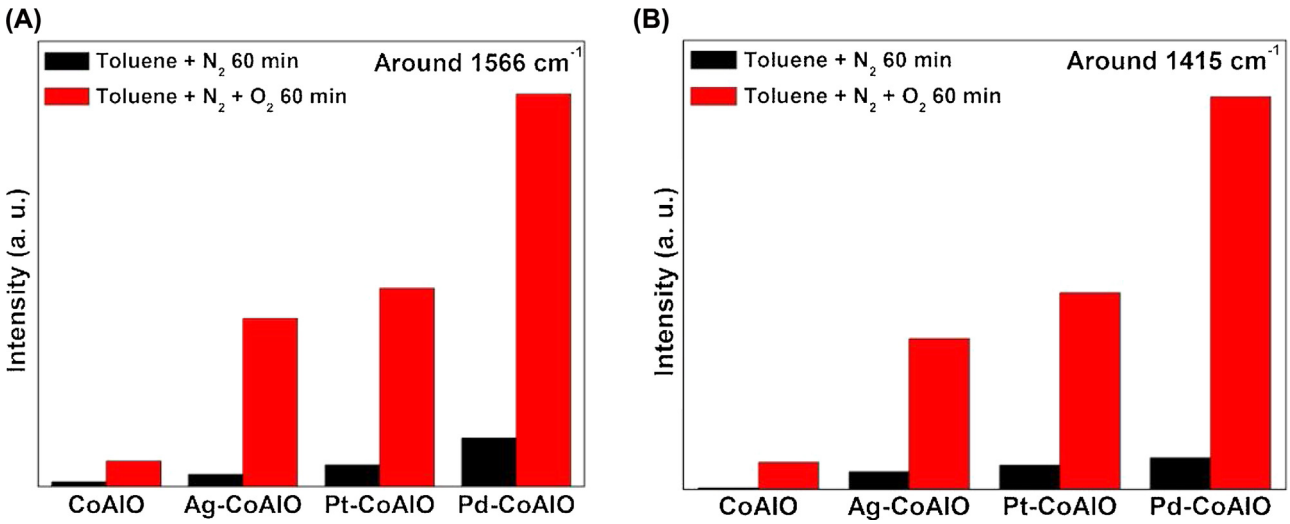

Fig. 14. Formation of benzoate species (indicated by bands area approximately 1566 and 1415 cm^{-1}) at 150 °C upon passing 500 ppm toluene + 20% O_2 + balance N_2 over CoAlO and N–CoAlO catalysts.

similar to the reported literature [20]. As shown in Fig 12A and Table S7, the reaction temperature (T_{10}, T_{50} and T_{90}) results suggest that the catalytic activity increased in the following order: MgAlO < CoAlO < Pd–MgAlO < Pd–CoAlO. Fig 12B and Table S7 indicate that the E_a values decreased in the following order: MgAlO (158.8 kJ/mol) > CoAlO (147.5 kJ/mol) > Pd–MgAlO (112.5 kJ/mol) > Pd–CoAlO (49.5 kJ/mol), which confirms the catalytic activities in the following order: MgAlO < CoAlO < Pd–MgAlO < Pd–CoAlO. It has been reported the Co^{3+} cations are the active species of the oxidation reaction, which can easily oxidize the reagent molecules [27]. At the same time, the Raman, H_2-TPR and XPS results indicates that the Co^{3+} cations can increase oxygen vancancy densities that directly participate in the adsorption, activation, and migration of oxygen [4d]. The above results reveal that (1) the cobalt in CoAlO and N–CoAlO play significant role in the toluene combustion and (2) CoAlO is not only the support of noble metals but also involved in the reaction process.

To investigate the role of PdO phase in the reaction process, we have compared the catalytic activities of Pd–CoAlO-N_2 (Pd–CoAl-LDHs were calcinated in nitrogen at 600 °C for 4 h) and Pd–CoAlO–Air (Pd–CoAl-LDHs were calcinated in air at 600 °C for 4 h). Initially, the characterization of Pd–CoAlO–N_2 has been carried out to confirm its structure. The XRD patterns show that no PdO crystalline phase has been detected in Pd–CoAlO–N_2 (Fig S11A), and the Raman spectra indicates that Pd–CoAlO–N_2 has the similar red shift to Pd–CoAlO–Air (Fig S11B). The characterization results reveal that Pd–CoAlO–N_2 has the similar structure to Pd–CoAlO–Air except the absence of PdO crystalline phase. Then, the comparison results of the catalytic activities over these two catalysts have been shown in Fig 13. As shown in Fig 13A and Table S8, the reaction temperature (T_{10}, T_{50} and T_{90}) results suggest that the catalytic activity increased in the following order: Pd–CoAlO–N_2 < Pd–CoAlO–Air. Fig 13B and Table S8 indicate that the E_a values decreased in the following order: Pd–CoAlO–N_2 (98.1 kJ/mol) > Pd–CoAlO–Air (49.5 kJ/mol), which confirms the catalytic activities in the following order: Pd–CoAlO–N_2 < Pd–CoAlO–Air. It has been reported that the PdO phase can activate the O^{2-} species of CoAlO [28]. At the same time, the O^{2-} species can also improve the reaction ability of the PdO phase; enhance the breakage of H_2, O_2 and NO bonds and strengthen the bonding ability of H, O, N and C atoms to the PdO phase [29]. In the reaction process, the active O^{2-} species around PdO are directly depleted and replenished by CoAlO support as a reservoir providing oxygen [30]. Finally, the above results reveal that (1) the PdO crystalline phase in Pd–CoAlO play dominant role in toluene combustion and (2) the PdO phase and CoAlO support participate cooperatively in the reaction process.

3.8. Reaction intermediates

The *in situ* DRIFTS experiments for CoAlO and N–CoAlO were carried out to determine the intermediate species and investigate the reaction mechanism for toluene combustion. The *in situ* DRIFTS were recorded as a function of time after 500 ppm toluene + balance N_2 or 500 ppm toluene + 20% O_2 + balance N_2 was introduced to the cell at 150 °C. The DRIFTS results for CoAlO and N–CoAlO are shown in Figs. S12–15 and Table S9. The bands at 3073 and 3034 cm^{-1} were assigned to the C-H stretching vibration bands of the aromatic rings. The band due to a phenylic C-H stretching vibration located at 3034 cm^{-1}, which is the most intense band in the spectrum of liquid- or gas-phase toluene, was reduced to a very weak shoulder near the band at 3073 cm^{-1}. This observation indicates the transformation of the methyl group because the stretching vibration of the aromatic C—H bands are known to be substituent sensitive and related to the Hammett parameter of the substituent [31]. The C—H stretching vibrations of the alkyl group were observed as weak bands located at 2934 and 2883 cm^{-1} for CoAlO and N–CoAlO. These bands can be assigned to the antisymmetric and symmetric stretching vibration of a methylene group, which is characteristic of a benzyl species. These bands disappeared with N_2 purging for 60 min, which indicates that all of the H atoms of the methyl group have been abstracted [32]. The aromatic system remained intact, and this result is based on the presence of ring vibrations at 1607–1601 and 1497 cm^{-1} [33]. The bands at 1566–1554 and 1425–1412 cm^{-1} are characteristic of the carboxylate group [32], indicating the formation of benzoate species. In addition, for CoAlO and N-CoAlO, different features of benzoate species adsorption were observed between toluene adsorption and toluene + O_2 adsorption, and the toluene + O_2 adsorption process significantly increased the formation of benzoate species compared to that of the toluene adsorption process. It is important to note that the bands located at 1677 and 1462 cm^{-1}, which were assigned to the typical bands of aldehydic species, have been observed for CoAlO. However, no such bands have been detected for N–CoAlO. Toluene combustion has been reported to proceed in

consecutive steps *via* benzylic, aldehydic and benzoate species [34]. For N–CoAlO, no characteristic bands corresponding to aldehydic species were detected, and only typical bands corresponding to benzoate species were observed, which indicates that the aldehydic species rapidly transformed to the benzoate species. However, for CoAlO, the characteristic bands of both the aldehydic and benzoate species were observed, indicating that the oxidation process stopped at the aldehydic intermediate over CoAlO. Fig. 14 summarizes the results for the formation of benzoate species (indicated by the bands approximately 1566 and 1415 cm^{-1}) at 150 °C. Therefore, in toluene with or without O_2, the increase in the formation of benzoate species occurs in the following order: CoAlO < Ag–CoAlO < Pt–CoAlO < Pd–CoAlO, which is consistent with the catalytic activity order of the catalysts. For the catalytic combustion to proceed at an appreciable rate, further transient studies need to be carried out at relatively higher temperatures (*i.e.*, 200 °C). The decreasing trend for the benzoate species shown in Fig. S16 indicates that the benzoate species are the primary intermediate species in the toluene combustion, and this species should be further oxidized by O_2 to the final products (*i.e.*, CO_2 and H_2O). This speculation is consistent with previously reported results for toluene combustion [32,35].

4. Conclusions

To summarize, a series of noble metal nanoparticles (*i.e.*, Ag, Pt and Pd NPs) have been successfully immobilized on CoAl-LDH layers using a simple and facile *in situ* redox process. In addition, the CoAl-LDHs and N–CoAl-LDHs were calcined in air at 600 °C to afford the corresponding CoAlO, Ag–CoAlO, Pt–CoAlO and Pd–CoAlO catalysts for toluene combustion.

The catalytic results for toluene combustion indicated that the catalytic activity increased in the following order: CoAlO < Ag–CoAlO < Pt-CoAlO < Pd–CoAlO. In combination with the catalytic and characterization results, the catalytic performance of the catalysts was associated with low temperature reducibility and surface Co^{3+} and O_{ads} species. The Pd–CoAlO catalyst exhibited the highest catalytic activity because it possesses the highest low temperature reducibility and the most abundant surface Co^{3+} and O_{ads} species. In addition, the noble metal NP sizes of N-CoAlO affected the catalytic activity for toluene combustion, and the existence of catalytically active PdO contributed to the excellent catalytic activity of the Pd–CoAlO catalyst for toluene combustion. The comparison experiments reveal that the PdO phase and CoAlO support play significant role in the toluene combustion and they participate cooperatively in the reaction process. In addition, the *in situ* DRIFTS results indicated that the benzoate species are the main intermediate species in toluene combustion, and these species should be further oxidized by O_2 to the final products (*i.e.*, CO_2 and H_2O). The highly homogeneous and thermally stable dispersion of Pd NPs as well as the efficient and catalytic stability of Pd–CoAlO provide great potential for their practical application.

Acknowledgments

This work is supported by the National Natural Science Foundations of China (Grant No. 21325731 & 21221004) and the National High Science & Technology Project of China (Grant No. 2013AA065304). This study is also supported by the State Environmental Protection Key Laboratory of Sources and Control of Air Pollution Complex.

Appendix A. Supplementary data

Supplementary data associated with this article can be found, in the online version, at http://dx.doi.org/10.1016/j.apcatb.2015.08.001

References

[1] H.S. Kim, T.W. Kim, H.L. Koh, S.H. Lee, B.R. Min, Appl. Catal. A: Gen. 280 (2005) 125–131.
[2] (a) J.J. Spivey, Ind. Eng. Chem. Res. 26 (1987) 2165–2180;
(b) J.N. Armor, Appl. Catal. B: Environ. 1 (1992) 221–256;
(c) K. Everaert, J. Baeyens, J. Hazard. Mater. 109 (2004) 113–139.
[3] (a) J. Deng, H. Dai, H. Jiang, L. Zhang, G. Wang, H. He, C.T. Au, Environ. Sci. Technol. 44 (2010) 2618–2623;
(b) B. Bai, H. Arandiyan, J. Li, Appl. Catal. B: Environ. 142–143 (2013) 677–683;
(c) S. Li, H. Wang, W. Li, X. Wu, W. Tang, Y. Chen, Appl. Catal. B: Environ. 166–167 (2015) 260–269.
[4] (a) A.K. Sinha, K. Suzuki, M. Takahara, H. Azuma, T. Nonaka, K. Fukumoto, Angew. Chem. 119 (2007) 2949–2952, Angew. Chem. Int. Ed. 46 (2007) 2891–2894;
(b) P. Li, C. He, J. Cheng, C.Y. Ma, B.J. Dou, Z.P. Hao, Appl. Catal. B: Environ. 101 (2011) 570–579;
(c) Y. Wang, C. Zhang, F. Liu, H. He, Appl. Catal. B: Environ. 142–143 (2013) 72–79;
(d) B. Bai, J. Li, ACS Catal. 4 (2014) 2753–2762;
(e) C. Chen, Q. Wu, F. Chen, L. Zhang, S. Pan, C. Bian, X. Zhang, X. Meng, F.S. Xiao, J. Mater. Chem. A 3 (2015) 5556–5562;
(f) S. Xie, J. Deng, S. Zang, H. Yang, G. Guo, H. Arandiyan, H. Dai, J. Catal. 322 (2015) 38–48.
[5] (a) P. Gélin, M. Primet, Appl. Catal. B: Environ. 39 (2002) 1–37;
(b) S.K. Ihm, Y.D. Jun, D.C. Kim, K.E. Jeong, Catal. Today 93–95 (2004) 149–154;
(c) K. Okumura, T. Kobayashi, H. Tanaka, M. Niwa, Appl. Catal. B: Environ. 44 (2003) 325–331;
(d) H.L. Tidahy, S. Siffert, J.F. Lamonier, R. Cousin, E.A. Zhilinskaya, A. Aboukais, B.L. Su, X. Canet, G. De Weireld, A. Frere, J.M. Giraudon, G. Leclercq, Appl. Catal. B: Environ 70 (2007) 377–383.
[6] (a) V. Rives, M.A. Ulibarr, Coord. Chem. Rev. 181 (1999) 61–120;
(b) X. Duan, D.G. Evans, Structure and Bonding, Springer-Verlag, Berlin Heidelberg, 2006, pp. 1–223;
(c) Q. Wang, D. O'Hare, Chem. Rev. 112 (2012) 4124–4155.
[7] P. Li, P.P. Huang, F.F. Wei, Y.B. Sun, C.Y. Cao, W.G. Song, J. Mater. Chem. A 2 (2014) 12739–12745.
[8] G. Fan, F. Li, D.G. Evans, X. Duan, Chem. Soc. Rev. 43 (2014) 7040–7066.
[9] N. Iyi, Y. Ebina, T. Sasaki, J. Mater. Chem. 21 (2011) 8085–8095.
[10] C. Chen, P. Gunawan, X.W. (David) Lou, R. Xu, Adv. Funct. Mater. 22 (2012) 780–787.
[11] (a) M. Nocchetti, A. Donnadio, V. Ambrogi, P. Andreani, M. Bastianini, D. Pietrella, L. Latterini, J. Mater. Chem. B 1 (2013) 2383–2393;
(b) B. Yang, Z. Yang, R. Wang, Z. Feng, J. Mater. Chem. A 2 (2014) 785–791.
[12] S. Huang, C. Zhang, H. He, Catal. Today 139 (2008) 15–23.
[13] (a) J.F. Lamonier, A.B. Boutoundou, C. Gennequin, M.J. Pérez-Zurita, S. Siffert, A. Aboukais, Catal. Lett. 118 (2007) 165–172;
(b) D.A. Aguilera, A. Pérez, R. Molina, S. Moreno, Appl. Catal. B: Environ. 104 (2011) 144–150;
(c) E. Genty, R. Cousin, S. Capelle, C. Gennequin, S. Siffert, Eur. J. Inorg. Chem. (2012) 2802–2811;
(d) A. Pérez, R. Molina, S. Moreno, Appl. Catal. A: Gen. 477 (2014) 109–116;
(e) R. Dula, R. Janik, T. Machej, J. Stoch, R. Grabowski, E.M. Serwicka, Catal. Today 119 (2007) 327–331;
(f) F. Kovanda, K. Jirátová, J. Rymeš, D. Koloušek, Appl. Clay Sci. 18 (2001) 71–80;
(g) L.A. Palacio, J. Velásquez, A. Echavarría, A. Faro, F.R. Ribeiro, M.F. Ribeiro, J. Hazard. Mater. 177 (2010) 407–413;
(h) C. Gennequin, S. Siffert, R. Cousin, A. Aboukaïs, Top. Catal 52 (2009) 482–491;
(i) K. Jirátová, J. Mikulová, J. Klempa, T. Klempa, T. Grygar, Z. Bastl, F. Kovanda, Appl. Catal. A: Gen. 361 (2009) 106–116.
[14] M. Paulis, H. Peyrard, M. Montes, J. Catal. 199 (2001) 30–40.
[15] J. Cheng, J. Yu, X. Wang, L. Li, J. Li, Z. Hao, Energy Fuels 22 (2008) 2131–2137.
[16] Q. Liu, L.C. Wang, M. Chen, Y. Cao, H.Y. He, K.N. Fan, J. Catal. 263 (2009) 104–113.
[17] (a) Y. Lou, L. Wang, Z. Zhao, Y. Zhang, Z. Zhang, G. Lu, Y. Guo, Y. Guo, Appl. Catal. B: Environ. 146 (2014) 43–49;
(b) I. Lopes, N. El Hassan, H. Guerba, G. Wallez, A. Davidson, Chem. Mater. 18 (2006) 5826–5828.
[18] V. Rives, Layered Double Hydroxides: Present and Future, Nova Science, New York, 2001.
[19] C. Rudolf, B. Dragoi, A. Ungureanu, A. Chirieac, S. Royer, A. Nastro, E. Dumitriu, Catal. Sci. Technol. 4 (2014) 179–189.
[20] Y. Du, Q. Jin, J. Feng, N. Zhang, Y. He, D. Li, Catal. Sci. Technol. 5 (2015) 3216–3225.
[21] K. Chen, S. Xie, A.T. Bell, E. Iglesia, J. Catal. 198 (2001) 232–242.

[22] H. Dai, A.T. Bell, E. Iglesia, J. Catal. 221 (2004) 491–499.
[23] H. Huang, D.Y.C. Leung, ACS Catal. 1 (2011) 348–354.
[24] Z. Huang, X. Gu, Q. Cao, P. Hu, J. Hao, J. Li, X. Tang, Angew. Chem. 124 (2012) 4274–4279, Angew. Chem. Int. Ed. 51 (2012) 4198–4203.
[25] S. Mukherjee, M.A. Vannice, J. Catal. 243 (2006) 108–130.
[26] (a) M. Alifanti, M. Florea, S. Somacescu, V.I. Parvulescu, Appl. Catal. B: Environ. 60 (2005) 33–39;
(b) C.T. Wong, A.Z. Abdullah, S. Bhatia, J. Hazard. Mater. 157 (2008) 480–489.
[27] X. Xie, Y. Li, Z.Q. Liu, M. Haruta, W. Shen, Nature 458 (2009) 746–749.
[28] Y. Wang, C. Zhang, F. Liu, H. He, Appl. Catal. B: Environ. 142–143 (2013) 72–79.
[29] Y. Xu, J. Greeley, M. Mavrikakis, J. Am. Chem. Soc. 127 (2005) 12823–12827.
[30] R. Xu, X. Wang, D. Wang, K. Zhou, Y. Li, J. Catal. 237 (2006) 426–430.
[31] L.J. Bellamy, The Infrared Spectra of Complex Molecules, 3rd ed., Chapman & Hall, London, 1975.
[32] S. Besselmann, E. Löffler, M. Muhler, J. Mol. Catal. A: Chem. 162 (2000) 401–411.
[33] (a) F. Roozeboom, M.C. Mittelmeijer-Hazeleger, J.A. Moulijn, J. Memeda, V.H.J. de Beer, P.J. Gellings, J. Phys. Chem. 84 (1980) 2783–2791;
(b) F. Hatayama, T. Ohno, T. Maruoka, H. Miyata, React. Kinet. Catal. Lett. 45 (1991) 265–269.
[34] (a) G. Busca, Catal. Today 27 (1996) 457–496;
(b) G. da Silva, C.C. Chen, J.W. Bozzelli, J. Phys. Chem. A 111 (2007) 8663–8676.
[35] H. Sun, Z. Liu, S. Chen, X. Quan, Chem. Eng. J. 270 (2015) 58–65.